

Stability of $Ti_3C_2T_x$ MXene Films and Devices under Clinical Sterilization Processes

Spencer R. Averbeck, Doris Xu, Brendan B. Murphy, Kateryna Shevchuk, Sneha Shankar, Mark Anayee, Marcelo Der Torossian Torres, Michael S. Beauchamp, Cesar de la Fuente-Nunez, Yury Gogotsi, and Flavia Vitale*



Cite This: *ACS Nano* 2023, 17, 9442–9454



Read Online

ACCESS |

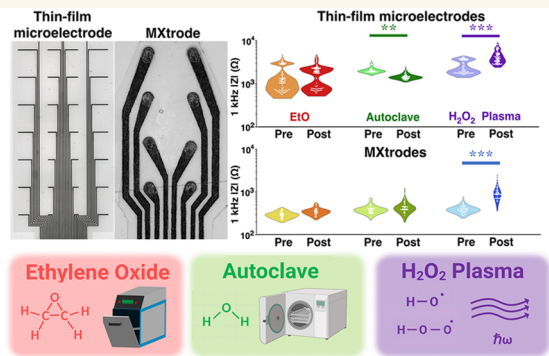
Metrics & More

Article Recommendations

Supporting Information

ABSTRACT: MXenes are being heavily investigated in biomedical research, with applications ranging from regenerative medicine to bioelectronics. To enable the adoption and integration of MXenes into therapeutic platforms and devices, however, their stability under standard sterilization procedures must be established. Here, we present a comprehensive investigation of the electrical, chemical, structural, and mechanical effects of common thermal (autoclave) and chemical (ethylene oxide (EtO) and H_2O_2 gas plasma) sterilization protocols on both thin-film $Ti_3C_2T_x$ MXene microelectrodes and mesoscale arrays made from $Ti_3C_2T_x$ -infused cellulose–elastomer composites. We also evaluate the effectiveness of the sterilization processes in eliminating all pathogens from the $Ti_3C_2T_x$ films and composites. Post-sterilization analysis revealed that autoclave and EtO did not alter the DC conductivity, electrochemical impedance, surface morphology, or crystallographic structure of $Ti_3C_2T_x$ and were both effective at eliminating *E. coli* from both types of $Ti_3C_2T_x$ -based devices. On the other end, exposure to H_2O_2 gas plasma sterilization for 45 min induced severe degradation of the structure and properties of $Ti_3C_2T_x$ films and composites. The stability of the $Ti_3C_2T_x$ after EtO and autoclave sterilization and the complete removal of pathogens establish the viability of both sterilization processes for $Ti_3C_2T_x$ -based technologies.

KEYWORDS: MXenes, bioelectronics, $Ti_3C_2T_x$, sterilization, wearables, implantable electrodes



Bioelectronic technologies are widely used in the clinical diagnosis and treatment of neurological and neuromuscular disorders.^{1–7} Since the introduction of implantable neuromodulators in the late 1960s, bioelectronic devices have predominantly relied on metals like platinum (Pt) and stainless steel to monitor and modulate the activity of excitable cells and tissues. These materials, however, pose significant challenges in realizing safe, stable, and functional interfaces with biological structures, primarily arising from the fundamental mismatch of their mechanical, electrochemical, and chemical properties.^{8–11} Propelled by the recognition of the tunable structure–function properties both at the molecular scale and in the assembled form, there has been a growing interest in leveraging nanostructured materials for applications in bioelectronics. Promising nanomaterials that have been explored include graphene,^{12–14} carbon nanotubes,^{15,16} nanodiamonds,¹⁷ and Pt nanorods,¹⁸ among others.

Two-dimensional metal carbides and nitrides (MXenes) are rapidly emerging as cost-effective and high-performance alternatives to noble metals for high-resolution, multiscale bioelectronics.^{19–21} MXenes are transition-metal carbides,

carbonitrides, and nitrides typically produced by selective etching of the A element, like aluminum, from the layered MAX-phase precursors, where M is an early transition metal and X is carbon or nitrogen. Among their properties, the high electrical conductivity,²² volumetric capacitance,²³ hydrophilicity,²⁴ biocompatibility,²⁵ and antibacterial nature^{26,27} make MXenes particularly suitable for bioelectronic applications. Liquid-phase processing of aqueous $Ti_3C_2T_x$ MXene dispersions has been successfully leveraged in several application-specific fabrication schemes to produce recording, stimulation, and biosensing devices. To date, $Ti_3C_2T_x$ -based bioelectronic technologies have been demonstrated in a number of applications, including wearable cardiac (electro-

Received: February 16, 2023

Accepted: May 9, 2023

Published: May 12, 2023



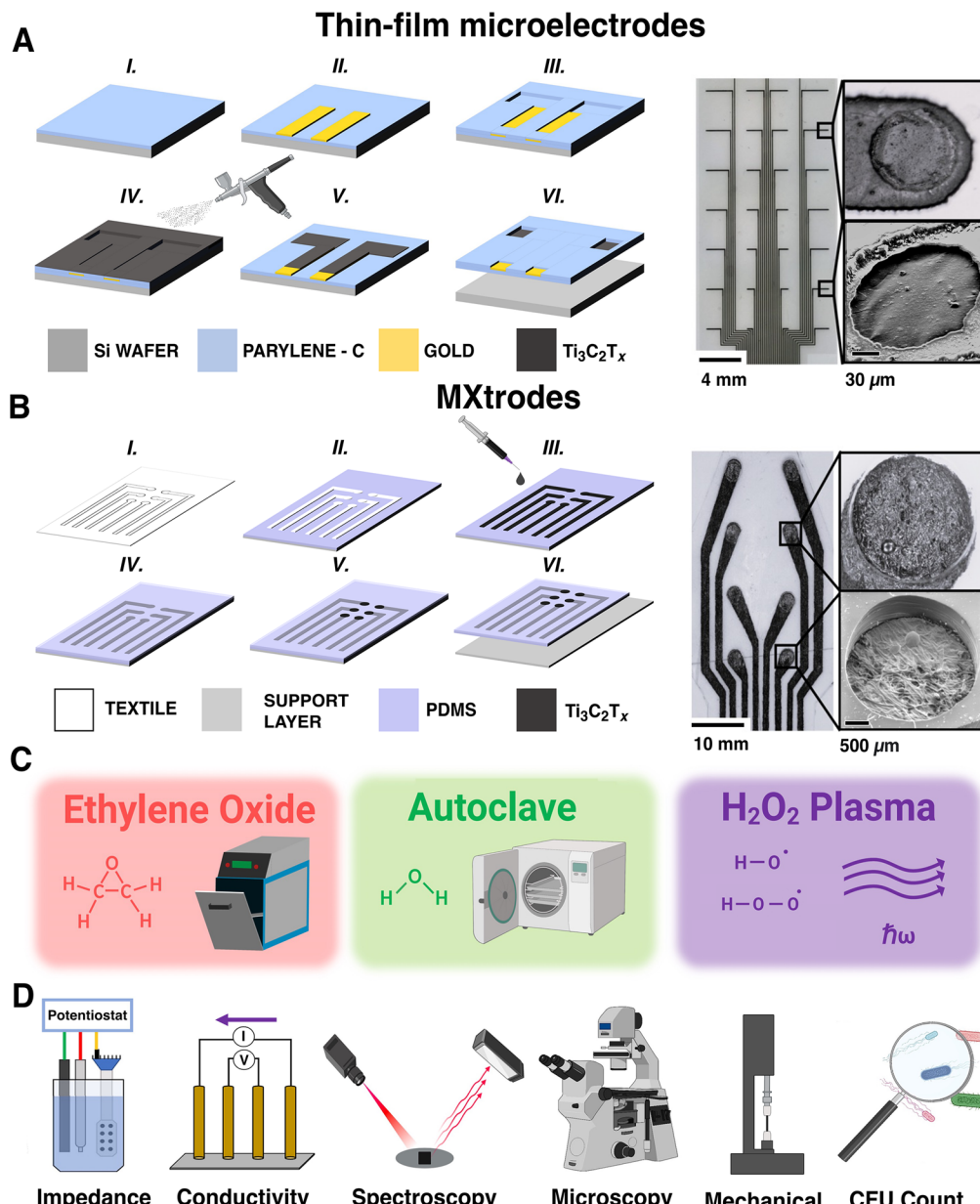


Figure 1. Overview of the study. (A, B) Left: schematics of fabrication process, right: bright-field microscopy and SEM images of completed arrays and contacts for (A) high-density $\text{Ti}_3\text{C}_2\text{T}_x$ MXene thin-film microelectrodes and (B) MXtrodex arrays. (C) Sterilization processes investigated in this work. (D) Schematics of the analysis methods used to evaluate the post-sterilization stability of $\text{Ti}_3\text{C}_2\text{T}_x$.

cardiography, ECG), muscle (electromyography, EMG), and brain (electroencephalography, EEG) electrodes,^{28–30} as well as invasive electrode arrays for neural recording and stimulation,^{31,32} detection of neurochemicals,^{33,34} and remote nongenetic neuromodulation.³⁵

As MXenes and other emerging nanomaterial-based technologies advance toward translation, their ability to withstand standard clinical sterilization processes to be rendered pathogen-free becomes of paramount importance and must be demonstrated. As dictated by the U.S. Centers for Disease Control (CDC) and other internationally accepted standards for medical device sterilization, any device or item intended to enter a sterile environment or tissue can pose a high risk of infection, thus requiring sterilization by either steam autoclave, H_2O_2 gas plasma, or ethylene oxide (EtO).^{36,37} Demonstrating robust stability of $\text{Ti}_3\text{C}_2\text{T}_x$ MXene

films and devices under these commonly implemented clinical sterilization procedures would thus mark an important milestone in the translational pathway of MXene-based medical technologies.

Here, we present a systematic investigation of the stability of $\text{Ti}_3\text{C}_2\text{T}_x$ MXene films and devices under EtO, steam autoclave, and H_2O_2 gas plasma sterilization. Specifically, we investigate thin films of $\text{Ti}_3\text{C}_2\text{T}_x$ spray-cast onto Parylene C to form microelectrode arrays,³² as well as devices made from laser-machined cellulose–polyester blends infiltrated with $\text{Ti}_3\text{C}_2\text{T}_x$.³⁰ We first evaluate the effects of sterilization on the electrical, electrochemical, structural, chemical, and mechanical properties of $\text{Ti}_3\text{C}_2\text{T}_x$ films and devices. Then, we demonstrate the effectiveness of the sterilization processes in rendering $\text{Ti}_3\text{C}_2\text{T}_x$ devices pathogen-free, by quantifying *E. coli* bacterial

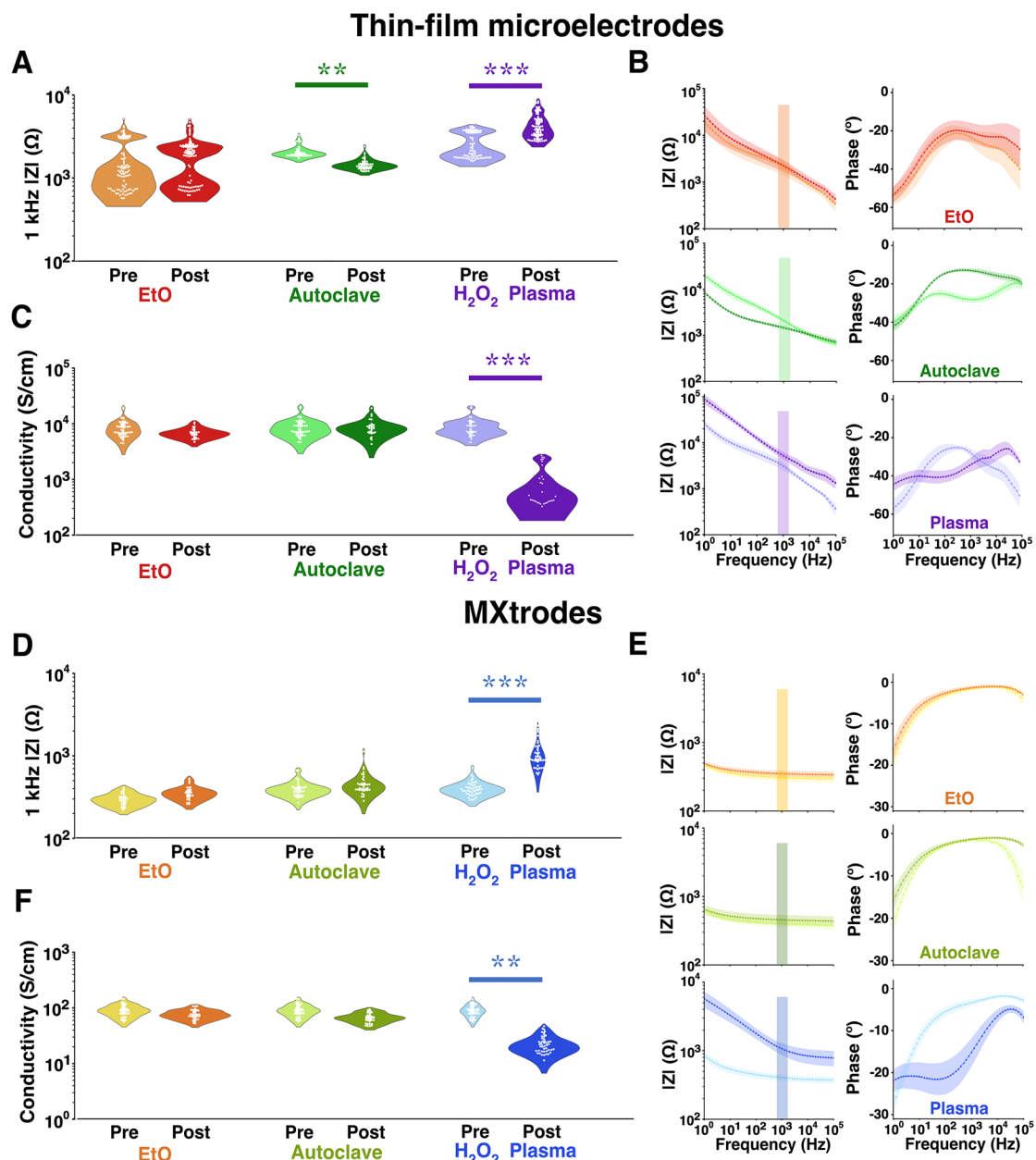


Figure 2. Electrochemical impedance and DC conductivity of sterilized devices. (A–C) Thin-film microelectrodes: (A) 1 kHz impedance modulus (EtO: 3 devices, $n = 96$ channels, autoclave: 2 devices, $n = 53$ channels, H_2O_2 plasma: 3 devices, $n = 86$ channels). (B) Full-band EIS impedance and phase spectra. (C) DC conductivity ($n = 30$ samples each). (D–F) MXtrodies: (D) 1 kHz impedance modulus (sample size: 5 devices each, $n = 40$ channels). (E) Full-band EIS impedance and phase spectra. (F) DC conductivity ($n = 45$ samples each). (*effect size > 1, **effect size > 2, ***effect size > 3). In (B) and (E) points are means, and shaded areas are standard deviations.

units in both device types over a 24 h post-sterilization incubation period.

RESULTS AND DISCUSSION

$Ti_3C_2T_x$ thin-film microelectrodes and cellulose–polyester– $Ti_3C_2T_x$ arrays (a.k.a. MXtrodies) were fabricated using previously established protocols, detailed in the Supporting Information (SI).^{30,32} Briefly, thin-film microelectrodes were arranged in a 4×8 grid (12.1 mm \times 28.1 mm) made of $Ti_3C_2T_x$ films (~ 1 mg/mL, 100 mL) spray-cast onto a 3.5- μ m-thick Parylene C film (Figure 1A). Then 100-nm-thick Ti/Au pads and interconnects were photolithographically defined and electron-beam deposited before a second 3.5- μ m-thick Parylene C layer was added to form the top encapsulation.³²

Electrode diameter and pitch are 100 μ m and 4 mm (in both directions, Figure S1). The thin-film microelectrodes were designed to provide high-resolution neural monitoring capabilities by leveraging a high density of microscale electrode contacts made on an ultrathin substrate (final device thickness: 7.0 ± 1.1 μ m, number of samples: $n = 8$). Cellulose–polyester– $Ti_3C_2T_x$ MXtrodies were composed of 2.5 mm contacts arranged in a 2×4 array (12.5 mm \times 32.5 mm) spaced 1 cm apart (Figures 1B and S2). The arrays were fabricated from a Texwipce cellulose–polyester blend textile infused with $Ti_3C_2T_x$ (~ 20 mg/mL) and were encapsulated on both sides with ~ 300 μ m polydimethylsiloxane (PDMS) layers (final device thickness: 820 ± 100 μ m, $n = 14$). The elemental composition of device contacts was qualitatively confirmed for

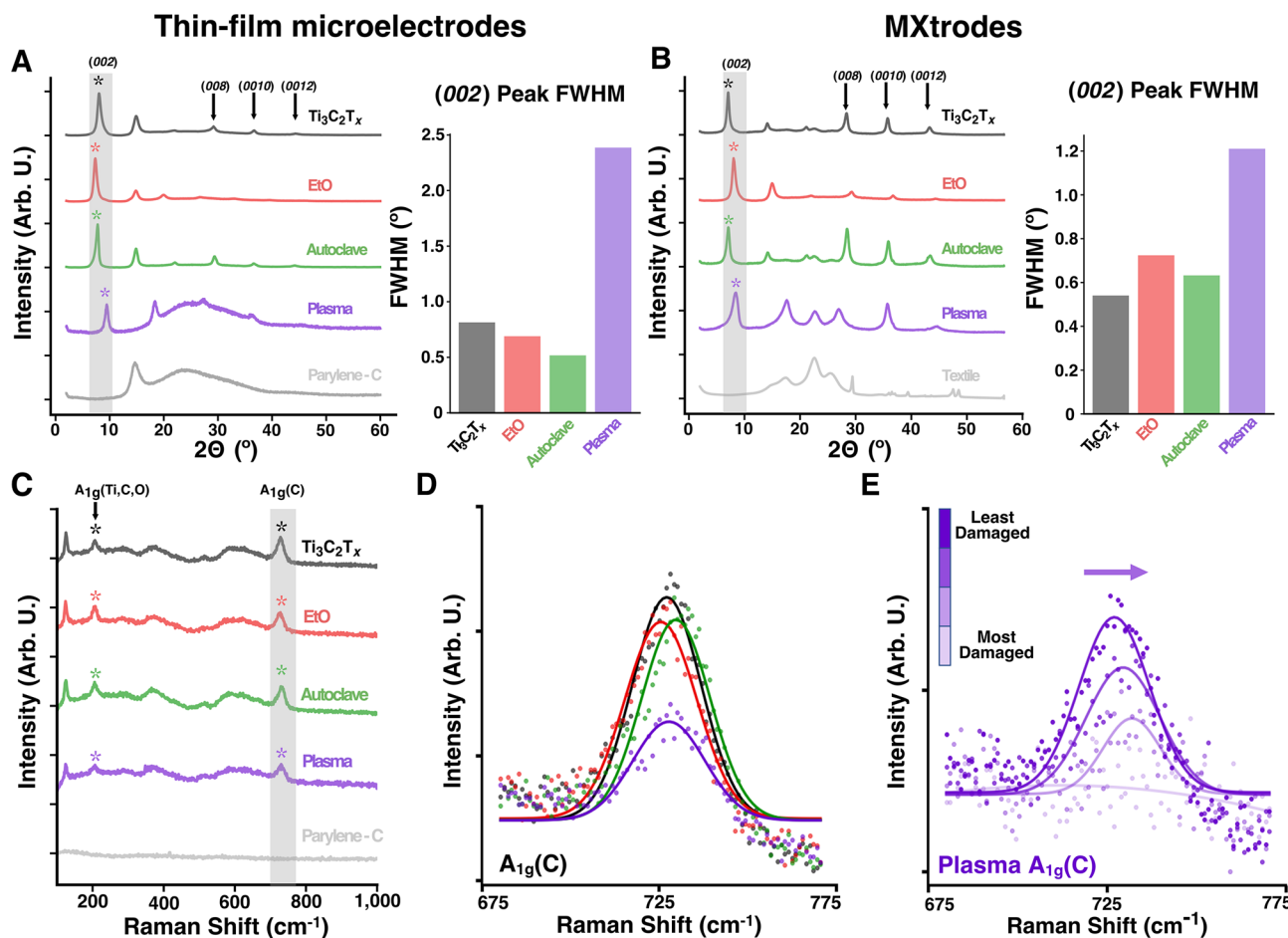


Figure 3. Raman and XRD analysis of pristine and sterilized devices. (A, B) Left: XRD patterns including pristine control and Parylene C or textile backgrounds. Right: fwhm of the (002) peak for (A) thin-film devices and (B) MXtrodess ($n = 2$ for each condition). (C) Raman spectra including pristine controls and Parylene C background for thin-film devices ($n = 2$ samples for each condition). (D) Normalized Gaussian-fitted $\text{A}_{1g}(\text{C})$ peak for thin-film devices. (E) Right-shifting normalized Gaussian-fitted $\text{A}_{1g}(\text{C})$ peak for increasingly visually damaged thin-film samples after H_2O_2 gas plasma sterilization.

both device form-factors using energy dispersive X-ray spectroscopy (EDX) measurements, which highlighted the elemental presence of $\text{Ti}_3\text{C}_2\text{T}_x$ as well as the encapsulating Parylene C for thin-film microelectrodes and PDMS for MXtrodess (Figure S3).

We subjected both types of devices to the following sterilization cycles using clinical equipment and standard cycle parameters: EtO, Anprolene AN74i, 12 h cycle, 2 h post-sterilization gas purge; steam autoclave, Primus PSS 500, up to 30 min cycle, 134 °C chamber temperature; H_2O_2 gas plasma, Sterrad NX 100, 47 min cycle, subambient pressure (Figure 1C). After each sterilization cycle, we evaluated the electrochemical and bulk conductivity effects of sterilization by collecting electrochemical impedance spectroscopy (EIS) and DC conductivity with a Gamry Reference 600 potentiostat and a Loresla-AX four-point probe, respectively. We further characterized the effects of sterilization on the structure, bulk, and surface chemistry of $\text{Ti}_3\text{C}_2\text{T}_x$ using X-ray diffraction (XRD), Raman spectroscopy, and X-ray photoelectron spectroscopy (XPS) for each device. Additionally, we used optical and scanning electron microscopy (SEM) to visualize the effects of sterilization on the devices and characterize the extent of film cracking and delamination of the $\text{Ti}_3\text{C}_2\text{T}_x$ from the underlying substrate at the exposed contact sites. For MXtrode composites, we also investigated the mechanical

properties of device samples in response to sterilization by monitoring the change in device resistance over the course of hundreds of continuous cyclic deformations (to induce bending) as well as with vertical tensile elongation to failure. Finally, we evaluated the effectiveness of the sterilization treatments at rapidly removing all pathogens from the devices by measuring the presence of *E. coli* bacterial colony forming units (CFU) counted over a 24 h incubation period at 37 °C (Figure 1D).

Electrochemical and Electrical Stability. As bioelectronics primarily rely on the electrochemical transduction of ionic currents in the body at the electrode–tissue interface, we first investigated the influence of sterilization on the electrochemical interface impedance of thin-film and MXtrode devices with EIS scans acquired in 0.01 M phosphate-buffered saline (PBS) before and after each sterilization cycle. For thin-film microelectrodes post-EtO, we did not observe a significant change in the impedance modulus at the reference frequency of 1 kHz (pre: $1.9 \pm 1.2 \text{ k}\Omega$, post: $2.1 \pm 1.1 \text{ k}\Omega$, with a nonsignificant effect size of 0.21, Figure 2A and Table S1). We also did not observe a significant change in impedance across the entire 10^2 – 10^5 Hz frequency range. Autoclave-sterilized thin-film arrays showed a significant decrease in impedance post-sterilization (pre: $2.1 \pm 0.3 \text{ k}\Omega$, post: $1.5 \pm 0.2 \text{ k}\Omega$, effect size: 2.54), which was accompanied by the disappearance of a

local minimum in the phase at 10^2 – 10^4 Hz, while the rest of the spectral response remained essentially unchanged (Figure 2B). This change in the phase behavior can be attributed to the evaporation of water intercalated between MXene layers in the films—possibly from ambient environmental humidity or aqueous EIS testing in the preautoclave exposure—and is further supported by a low d -spacing value of 11.4 \AA post-sterilization (Table S2). In contrast, H_2O_2 gas plasma sterilized devices showed a significantly higher impedance after sterilization (pre: $2.8 \pm 1.0\text{ k}\Omega$, post: $4.9 \pm 1.7\text{ k}\Omega$, effect size: 3.10) and a capacitive shift in the broadband phase response. H_2O_2 -sterilized thin-film devices also showed a decrease in their electronic properties with $>10\times$ DC conductivity loss (pre: $9.0 \pm 3.3 \times 10^3\text{ S cm}^{-1}$, post: $9.2 \pm 7.8 \times 10^2\text{ S cm}^{-1}$, effect size: 3.00). On the other hand, DC conductivity of $\text{Ti}_3\text{C}_2\text{T}_x$ films remained unchanged after EtO (pre: $8.9 \pm 3.2 \times 10^3\text{ S cm}^{-1}$, post: $7.1 \pm 1.4 \times 10^3\text{ S cm}^{-1}$, effect size: 0.698) and autoclave sterilization (pre: $8.9 \pm 3.1 \times 10^3\text{ S cm}^{-1}$, post: $8.7 \pm 3 \times 10^3\text{ S cm}^{-1}$, effect size: 0.087, Figure 2C and Table S3).

MXtrode devices also showed similar EIS and DC conductivity responses in each of the tested conditions. The impedance modulus and phase behavior of sterilized MXtrodies were stable after both EtO (pre: $300 \pm 60\text{ }\Omega$, post: $350 \pm 60\text{ }\Omega$, effect size 0.887) and autoclave sterilization (pre: $400 \pm 80\text{ }\Omega$, post: $460 \pm 150\text{ }\Omega$, effect size: 0.872, Figure 2D). Interestingly, the phase response of the MXtrode devices did not show evidence of intercalated water removal after autoclave sterilization and appeared to be unaffected by the treatment cycle, with a d -spacing of 12.5 \AA both before and after sterilization. This could be caused by the composite morphology, where the cellulose–polyester–PDMS matrix inhibits the ingress of water between the $\text{Ti}_3\text{C}_2\text{T}_x$ flakes, as previously suggested.³⁸ Consistent with the thin-film device response, however, H_2O_2 gas plasma strongly affected the electrochemical interface of MXtrodies, with the impedance modulus increasing from $400 \pm 80\text{ }\Omega$ to $1100 \pm 410\text{ }\Omega$ (significant effect size of 10.1) and the phase response again shifting to lower angles (Figure 2E). We also evaluated potential size effects in the impedance response by exposing MXtrode devices with 1 mm and 5 mm contact size to the same sterilization conditions, but we did not find any significant difference in effect compared to the 2.5 mm devices (Figure S4), although we did see the overall magnitude of impedance increase with decreasing electrode diameter regardless of sterilization, as expected.^{39,40} DC conductivity measures also had similar trends in the effects of sterilization on the 2.5 mm MXtrodies with nonsignificant changes after EtO (pre: $90 \pm 20\text{ S cm}^{-1}$, post: $77 \pm 14\text{ S cm}^{-1}$, effect size: 0.490, Figure 2F) and autoclave sterilization (pre: $92 \pm 21\text{ S cm}^{-1}$, post: $68 \pm 13\text{ S cm}^{-1}$, effect size: 0.791), but a significant $>3\times$ drop in conductivity after exposure to H_2O_2 gas plasma (pre: $90 \pm 22\text{ S cm}^{-1}$, post: $23 \pm 8\text{ S cm}^{-1}$, effect size: 2.21).

XRD and Raman Analysis of $\text{Ti}_3\text{C}_2\text{T}_x$ Films and Devices. To confirm that the structure and chemical composition of $\text{Ti}_3\text{C}_2\text{T}_x$ thin films and composites were unaffected by EtO and autoclave, but also to further elucidate the mechanisms of H_2O_2 gas plasma-induced degradation, we collected XRD patterns and Raman spectra for each sterilization condition and quantitatively compared the results against (1) pristine (i.e., non-sterilized) $\text{Ti}_3\text{C}_2\text{T}_x$ samples and (2) the background spectra of the substrate. In the XRD patterns, we noted the presence of the characteristic (00l)

peaks of $\text{Ti}_3\text{C}_2\text{T}_x$ MXene for all pristine and sterilized samples in both device form factors, indicative of out-of-plane stacking of MXene flakes (Figure 3A and 3B).⁴¹ We further calculated the full width at half-maximum (fwhm) of the dominant (002) peak for each sample to probe the flake alignment and interlayer spacing variations in the sterilized samples.⁴² For both device types, the fwhm did not vary significantly after either EtO or autoclave sterilization, indicating no change in the flake alignment. Furthermore, the increased intensity of high-order (00l) peaks in the autoclaved samples suggests a regular spacing between MXene layers and no negative effect of this treatment on the film structure. Only a minor expansion of the interlayer spacing was observed for the EtO-sterilized thin films (from 10.9 to 12.1 \AA), which notably did not affect the post-sterilization electrochemical behavior. H_2O_2 gas plasma sterilized thin films and MXtrodies, however, showed a significant increase in the fwhm of the (002) peak, which is indicative of a decreased structural order and, possibly, more anisotropic spacing of the $\text{Ti}_3\text{C}_2\text{T}_x$ flakes.^{43,44} Further, the XRD patterns of the H_2O_2 gas plasma samples showed a broad scattering background similar to the Parylene C layer for the thin films and the strong peak at $\sim 23^\circ$ similar to the textile for the MXtrodies, which both indicate some loss of $\text{Ti}_3\text{C}_2\text{T}_x$ layers, damage and sputtering of the substrate layers, or formation of amorphous degradation products. Likely, loss of interlayer water and sintering of the films after gas plasma sterilization resulted in the upshift of the (002) peak, which is further supported by the decrease in the d -spacing after H_2O_2 gas plasma treatment.

Raman spectra of the pristine and sterilized $\text{Ti}_3\text{C}_2\text{T}_x$ MXene thin films and MXtrode samples (Figures 3C and S5) showed the characteristic $\text{Ti}_3\text{C}_2\text{T}_x$ peaks, including the $E_{1g}(\text{C})$ in-plane resonance at $\sim 120\text{ cm}^{-1}$ and both $A_{1g}(\text{Ti}, \text{C}, \text{O})$ and $A_{1g}(\text{C})$ out-of-plane peaks at $\sim 205\text{ cm}^{-1}$ and $\sim 730\text{ cm}^{-1}$, respectively.⁴⁵ Raman spectra were analyzed by normalizing the $A_{1g}(\text{C})$ peak in each spectrum by its maximum and fitting it with a Gaussian curve to compare the amplitude and peak center of the fitted $A_{1g}(\text{C})$ peaks and calculate the normalized fwhm. For both EtO and autoclave sterilized samples, there was no significant change in the $A_{1g}(\text{C})$ peak amplitude or fwhm compared with the pristine MXene. There was, however, a significant increase in the fwhm and decrease in the $A_{1g}(\text{C})$ peak amplitude that was only seen in the H_2O_2 gas plasma sterilized samples, likely caused by surface degradation and a removal of MXene layers during the sterilization cycle (Figures 3D, S6, and S7). Indeed, when scanning at shift values $>1000\text{ cm}^{-1}$ there were large D and G band peaks indicative of amorphous carbons between 1100 and 1700 cm^{-1} formed upon MXene degradation in the H_2O_2 gas plasma thin-film samples, compared to much smaller peaks in EtO and autoclave samples (Figure S8A). Furthermore, in a subset of H_2O_2 gas plasma thin-film samples that became visually more damaged, the $A_{1g}(\text{C})$ peak trended toward lower amplitudes and right-shifted to higher wavelengths (from 727 cm^{-1} to 732 cm^{-1} , Figure 3E), which has been shown to be caused by a decrease in the MXene layer thickness^{44,46} and could potentially indicate the onset of $\text{Ti}_3\text{C}_2\text{T}_x$ oxidation.⁴⁷ In addition to the $A_{1g}(\text{C})$ peak, other characteristic Raman signatures of $\text{Ti}_3\text{C}_2\text{T}_x$ gradually attenuate with increasing level of visual damage, including the $A_{1g}(\text{Ti}, \text{C}, \text{O})$ and $E_{1g}(\text{C})$ peaks (Figure S8B). However, despite the visible lightening in color, surface damage, and right-shifted $A_{1g}(\text{C})$ peak, there were no signs of rutile or anatase titanium oxide (TiO_2) on any of the

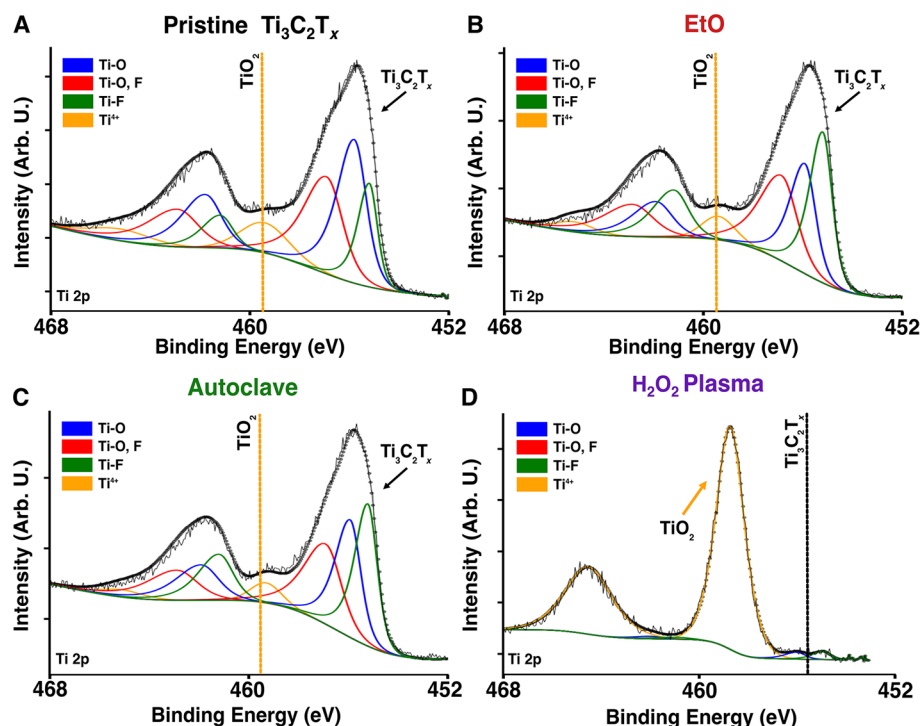


Figure 4. XPS of pristine and sterilized devices. (A–D) Ti 2p XPS spectra of thin-film microelectrodes (A) before and (B–D) after sterilization with EtO, autoclave, and H_2O_2 gas plasma, respectively.

Raman spectra collected for H_2O_2 -sterilized thin-film arrays and MXtrodies, despite the higher sensitivity of Raman to the formation of nanoscale TiO_2 compared to XRD.^{44,48} This suggests that the bulk chemistry of $\text{Ti}_3\text{C}_2\text{T}_x$ in the devices is unaffected by the exposure to H_2O_2 gas plasma. Moreover, the visible damage in the case of H_2O_2 plasma treatment was confined predominantly to the surface of the samples. Therefore, since the penetration depth of light into $\text{Ti}_3\text{C}_2\text{T}_x$ films is several microns with an excitation wavelength of 785 nm,⁴⁹ the presence of $\text{Ti}_3\text{C}_2\text{T}_x$ peaks in the Raman spectra of the H_2O_2 plasma treated films indicates that the majority of the damage did not exceed ~ 10 s of nanometers. This suggests that the $\text{Ti}_3\text{C}_2\text{T}_x$ is being continuously oxidized and etched away directly at the surface rather than throughout the bulk of the material.

XPS Analysis Confirms Oxidation after H_2O_2 Gas Plasma Sterilization. To characterize the chemical composition of the sterilized samples and investigate the possible presence of surface TiO_2 as a driving mechanism for $\text{Ti}_3\text{C}_2\text{T}_x$ degradation in H_2O_2 gas plasma sterilized samples, we collected XPS spectra for EtO, autoclave, and H_2O_2 gas plasma sterilized thin films and MXtrodies and compared them to pristine samples. For pristine samples and those sterilized with EtO and autoclave, the Ti 2p spectra show three pairs of doublets attributed to Ti with $-\text{O}$ and $-\text{F}$ surface terminations indicative of properly synthesized $\text{Ti}_3\text{C}_2\text{T}_x$ MXene and with less than $\sim 10\%$ of the spectra stemming from TiO_2 (doublet at ~ 459 and ~ 465 eV, Figures 4A–C and S9A and Table S4).^{50,51} Similarly, the C 1s spectra clearly show one peak attributed to C–Ti bonding, indicative of pristine MXene, and other peaks attributed to adventitious carbon contamination on the surface (Figure S9C).⁵¹ After H_2O_2 gas plasma sterilization, however, the components attributed to $\text{Ti}_3\text{C}_2\text{T}_x$ in the Ti 2p and C 1s spectra completely disappear (Figure 4D), and the survey spectra indicate only titania, amorphous

carbon, and silica remain, confirming surface oxidation (Figures 4D and S9A).^{44,52} The increase of the Si 2s and Si 2p peaks in the survey spectra, presumably from silica, is indicative of the exposed substrate for the thin-film samples, which again indicate the loss of $\text{Ti}_3\text{C}_2\text{T}_x$ flakes in plasma-sterilized samples, consistent with XRD and Raman results. Considering that XPS probing depth is less than 10 nm, and titania was only identified in XPS but not in Raman spectra, our findings suggest that only the surface layers—between 10 and 100 nm—are oxidized and the remaining $\text{Ti}_3\text{C}_2\text{T}_x$ is intact. Moreover, the exposed substrate indicates that damage is not homogeneous throughout the entire surface and some spots might be more damaged than others.

Optical and SEM of Thin-Film Microelectrode and MXtrode Contacts. The degradation of H_2O_2 gas plasma sterilized devices was also visually apparent. The 100 μm thin-film microelectrode and 2.5 mm MXtrode contacts were visibly lighter in color and showed clear removal of $\text{Ti}_3\text{C}_2\text{T}_x$ on and around the contact site post-sterilization (Figure 5). Additionally, SEM measurements of the contact surfaces revealed that there was clear cracking of the $\text{Ti}_3\text{C}_2\text{T}_x$ films for both thin-film microelectrode and MXtrode devices that were sterilized with H_2O_2 gas plasma along with a relative increase in elemental oxygen in the EDX spectra (Figure S10). Notably, however, there was no apparent delamination of the encapsulating substrate visible for either device type, and both Parylene C and PDMS layers appeared undamaged. In contrast to the visible damage incurred after gas plasma sterilization, however, EtO- and autoclave-sterilized thin-film and MXtrode contacts remained visually unaffected and showed no sign of $\text{Ti}_3\text{C}_2\text{T}_x$ cracking or delamination on or around the exposed contacts, similar to the pristine, unsterilized contacts.

Mechanical Stability of MXtrodies to Cyclic Bending and Tensile Testing. Additional characterization of the effects of sterilization was performed by assessing the

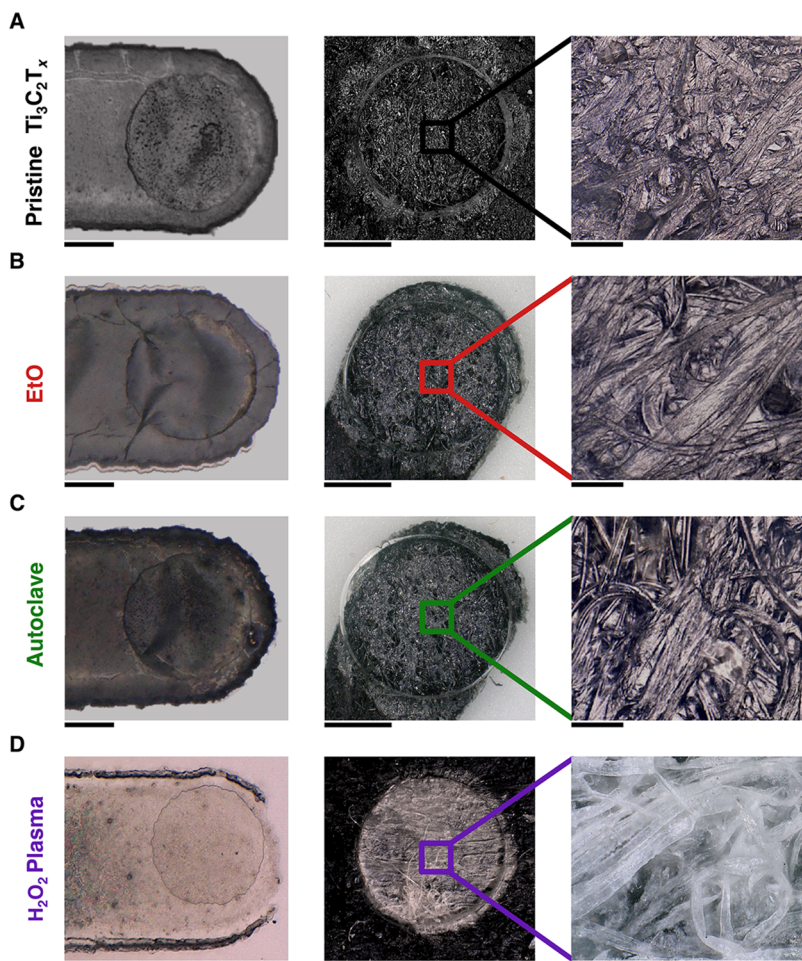


Figure 5. Optical microscopy of pristine and sterilized device contacts. (A–D) Left: bright-field microscopy image of thin-film microelectrode contacts in pristine and sterilized conditions. Scale bar: 50 μm . Middle: bright-field microscopy image of MXtrode contacts in all conditions. Scale bar: 1.25 mm. Right: zoom-in of individual cellulose–polyester fibers coated in $\text{Ti}_3\text{C}_2\text{T}_x$ MXene for (A) pristine, (B) EtO, (C) autoclave, and (D) H_2O_2 gas plasma sterilized devices. Scale bar: 100 μm .

mechanical stability of MXtrode composites in response to cyclic bending and vertical tensile stress to failure. Briefly, cyclic deformation was performed over 300 cycles on pristine and sterilized sample MXtrode composites (5 mm \times 5 cm) to induce a bending radius of \sim 5 mm. While the measured change in resistance from pre- to post-bending remained low for pristine, EtO-sterilized, and autoclave-sterilized samples (10–16%), there was a large (>130%) increase in the relative resistance of H_2O_2 gas plasma sterilized samples after bending, likely caused by a combination of the degraded electrical performance and crack formation (Figure S11). Tensile stress strain measurements of the MXtrode samples were consistent in magnitude to those previously reported³⁰ and appear to be driven—in all samples—by the mechanical properties of the encapsulating PDMS in the linear regime. The relative failure points for each sample condition appeared to be driven by local variations or defects in the PDMS thickness and did not seem to be affected by sterilization.

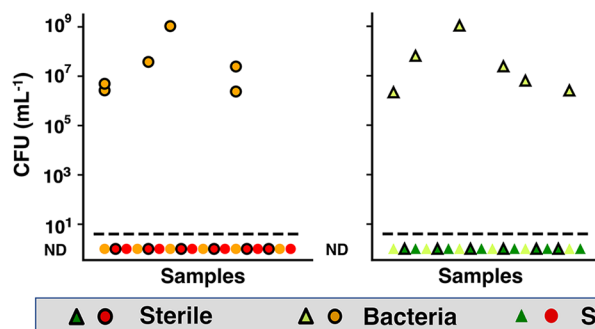
Sterilization Is Effective at Rapidly Eliminating Pathogens from $\text{Ti}_3\text{C}_2\text{T}_x$ Devices. Finally, to evaluate the efficacy of EtO and autoclave at rapidly removing any and all bacterial pathogens adhered to the devices in a single sterilization cycle, we inoculated *E. coli* onto the devices prior to exposure to the sterilization cycles. After sterilization, we incubated all samples in culture media at 37 °C and then

measured CFUs and optical density at 600 nm wavelength (OD_{600}) over the following 24 h. Samples exposed to *E. coli* that were not sterilized showed bacterial contamination and proliferation at all six time points during the 24 h of the experiment (Figures 6 and S12). Notably, this high volume of bacteria in unsterilized samples is not related to the antibacterial properties of $\text{Ti}_3\text{C}_2\text{T}_x$ directly, but rather is a control indicating that complete devices ($\text{Ti}_3\text{C}_2\text{T}_x$, PDMS, Parylene C, Au, cellulose-textiles) that are not sterilized will not be *clinically* sterile or safe for patient use. For all of the samples inoculated and sterilized, however, both the bacterial count and optical density were below the detection limit threshold (ND) at all time points. These findings demonstrate that $\text{Ti}_3\text{C}_2\text{T}_x$ thin-film microelectrodes and MXtrode composites can be effectively and completely sterilized by EtO and autoclave and rapidly rendered pathogen-free for clinically safe use in wearable and implantable devices.

CONCLUSION

Here, we have investigated the effects and efficacy of the three most common sterilization techniques on $\text{Ti}_3\text{C}_2\text{T}_x$ thin films and textile–PDMS composites assembled in the form of electrode arrays. Our studies reveal that EtO and autoclave sterilization do not cause any change in the crystalline structure, mechanical strength, or the electronic/electro-

Thin-film microelectrodes



MXtrodies

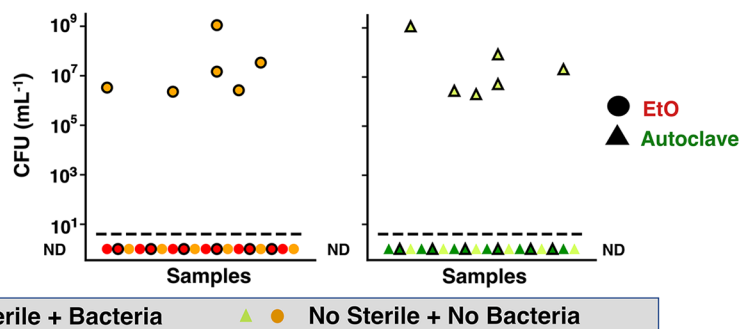


Figure 6. Efficacy of EtO and autoclave sterilization. CFU counts at all time points (0, 0.5, 1, 2, 4, and 24 h) for different combinations of sterility and bacterial inoculation of thin-film microelectrodes and MXtrodies. All samples below the dashed line had non-detectable bacterial counts. ND: non-detectable ($n = 6$ samples for each condition).

chemical properties of $\text{Ti}_3\text{C}_2\text{T}_x$. Interestingly, autoclave sterilized thin-film devices showed a slight, but consistent improvement in electrochemical impedance and disappearance of double-peak phase shifts in full EIS spectra, likely due to the removal of intercalated water. Exposure to 45 min cycles of H_2O_2 gas plasma sterilization, however, resulted in severe degradation of $\text{Ti}_3\text{C}_2\text{T}_x$ films and composites, evidenced by a significant drop in electrical conductivity, decreased flake alignment, cracking, and $\text{Ti}_3\text{C}_2\text{T}_x$ delamination from the substrates. While there was no presence of rutile or anatase TiO_2 peaks in XRD patterns or Raman spectra, surface chemical analysis with XPS indicated that MXene is oxidized to TiO_2 at least to within 10 nm from the surface, where the H_2O_2 radicals and ultraviolet (UV) excitation are likely driving $\text{Ti}_3\text{C}_2\text{T}_x$ degradation. The functional and structural damage from H_2O_2 gas plasma sterilization treatment is not specific to $\text{Ti}_3\text{C}_2\text{T}_x$ and has already been independently found to damage other common bioelectronic materials, such as PEDOT:PSS, indicating that H_2O_2 gas plasma sterilization is not a viable option with many emerging nanomaterial and organic bioelectronics.⁵³ Furthermore, H_2O_2 gas plasma is not compatible with common electronic components, such as connectors and head-stage amplifiers, or with many active bioelectronic technologies.⁵⁴ Finally, we demonstrated that EtO and autoclave sterilization are effective at completely and rapidly removing all common and significantly harmful pathogens like *E. coli* bacteria from $\text{Ti}_3\text{C}_2\text{T}_x$ thin films and composites within a single sterilization cycle. As synthesis and functionalization of $\text{Ti}_3\text{C}_2\text{T}_x$ play an important role in determining its stability and resistance to oxidation, future work should elucidate the effects of different synthesis processes and terminal groups on $\text{Ti}_3\text{C}_2\text{T}_x$ resistance to H_2O_2 gas plasma.⁵⁵ Ultimately, our findings indicate that common sterilization processes widely adopted in clinical and research settings, such as EtO and autoclave, do not alter $\text{Ti}_3\text{C}_2\text{T}_x$ MXene devices and thus can be integrated in processing, manufacturing, and surgical workflows for wearables and invasive implants, paving the way for the future translation of $\text{Ti}_3\text{C}_2\text{T}_x$ MXene bioelectronics and other medical technologies.

METHODS

Ti₃C₂T_x MXene Synthesis. Suspensions of $\text{Ti}_3\text{C}_2\text{T}_x$ MXene were produced and provided by MuRata Manufacturing, Co., Ltd. Large $\text{Ti}_3\text{C}_2\text{T}_x$ flakes ($\sim 2 \mu\text{m}$ lateral size) were synthesized using the

minimally intensive layer delamination (MILD) method, where the Al is etched from the Ti_3AlC_2 powder (MAX phase) with a combination of 12 M LiF and 9 M HCl.²⁴ $\text{Ti}_3\text{C}_2\text{T}_x$ MXene suspensions were stored in a large glass vial at 4 °C until use.

Device Fabrication. Thin-film microelectrodes were fabricated as follows from previously established protocols.³² On a 4 in. silicon wafer, 3.5- μm -thick Parylene C was deposited via chemical vapor deposition. Photolithography with negative resist (NR-71 3000p) was used to pattern conductive back-end channels of 10 nm/90 nm Ti/Au, deposited using electron beam deposition, and residual metal was lifted-off using an organic solvent. Next, an anti-adhesion cleaning solution was spun on the wafer to prevent adhesion of overlaid Parylene C layers, followed by the deposition of a 3- μm -thick sacrificial Parylene C layer. The second of three photolithography processes then outlined the 32 electrode contacts, and reactive ion etching (RIE) using O_2 plasma exposed the base Parylene C layer in these locations. Once the electrode contacts were exposed by the plasma etching, spray coating the 100 mL of dilute $\text{Ti}_3\text{C}_2\text{T}_x$ MXene ($\sim 1 \text{ mg mL}^{-1}$) onto the wafers was carried out using a hand-held, commercially available airbrush (Gravity Double Action Tattoo Art Model) from a distance of ~2 feet above the surface of the wafers at an angle of ~45° from horizontal. The $\text{Ti}_3\text{C}_2\text{T}_x$ MXene used was provided by MuRata Manufacturing as a stock 20 mg/mL, which we diluted to 1 mg/mL for spray coating with DI water. The dilution was homogenized by brief (~30 s) sonication prior to spray coating. The working spray coating pressure was held constant at 40 psi, and a 0.2 mm diameter nozzle was used. Spray coating was performed in a fume hood with the wafer set on a hot plate heated to 150 °C during the entire coating process. The angle of the spray nozzle was rapidly rastered left to right across the wafer repeatedly throughout spray coating, and the entire wafer was rotated 90° three times during the coating to ensure an even film distribution. After coating, the wafer was placed in an 80 °C oven for 30 min to bake out any residual water from the MXene films on the wafers. Once the $\text{Ti}_3\text{C}_2\text{T}_x$ MXene films had dried on the wafers, the sacrificial Parylene C layer was peeled up to leave $\text{Ti}_3\text{C}_2\text{T}_x$ MXene only at the 32 contact sites. A final 3.5 μm top-encapsulating Parylene C layer was deposited on the wafer, the device shape and exposed connections were photolithographically defined, and completed devices were peeled off the wafer after a final RIE. Devices were stored in a N_2 gas desiccator after peel-off and before use, to prevent MXene film oxidation.

MXtrodies were fabricated using a previously established protocol.³⁰ First, the stock 30 mg mL^{-1} suspensions were diluted to 20 mg mL^{-1} . Then, the array geometries were laser-patterned into a Texwipe nonwoven, hydrogenated cellulose–polyester blend substrate with a CO_2 laser. The electrode cutouts were then adhered with Adapt 3M medical adhesive spray to a ~300- μm -thick degassed and cured PDMS (SYLGARD 184, 10:1 ratio) sheet, which served as an underlying encapsulation layer. The woven electrode geometries were next inked with $\text{Ti}_3\text{C}_2\text{T}_x$ and placed in an 80 °C oven to bake for 1 h.

After inking and drying, back-end connectors were attached with CircuitWorks two-part conductive silver epoxy, to interface with the recording instrumentation. A final $\sim 300\text{-}\mu\text{m}$ -thick encapsulation layer was formed by pouring PDMS over the electrode arrays, followed by 10 min of degassing and 1 h of curing in the oven at 80°C . The encapsulated devices were then cut away from the PDMS sheet into their final form. Finally, to expose the electrode contacts, the PDMS was cut out with 1, 2.5, or 5 mm biopsy punches.

Sterilization Protocols. Ethylene oxide samples were sterilized in a Anprolene AN74*i* machine, using a single (12 h cycle) Anprolene EtO ampule to deliver the gas sterilization. All EtO samples were packaged in commercial steam and EtO sterilization wrapping, with an Anprolene biological dosimeter indicator and a Humidichip humidity chip. Samples were run under a 12 h cycle for all experiments. Autoclave samples were sterilized in a Primus PSS 500 autoclave machine. MXtrode and thin-film devices were packaged in commercial steam and EtO sterilization wrapping with indicator tape placed on the wall of the wrapping. Samples were steam sterilized using the vacuum cycle at 134°C for 30 min with a 20 min drying time. All H_2O_2 plasma sterilized MXtrode and thin-film microelectrode samples were packaged in Tyvek low-temperature pouches prior to sterilization. H_2O_2 sterilization was performed in a Sterrad NX 100 plasma sterilization tool for ~ 45 min cycles. The temperature of the H_2O_2 chamber did not exceed 50°C .

Electrochemical Impedance Spectroscopy. EIS of $\text{Ti}_3\text{C}_2\text{T}_x$ MXtrodies and thin-film microelectrodes was acquired with a Gamry Reference 600 potentiostat (Gamry Instruments) in room temperature 0.01 M PBS (pH 7.4). The measurements were collected in a three-electrode cell, with the MXtrode or thin-film microelectrode contact as the working electrode, a long graphite rod (Bio-Rad Laboratories, Inc.) serving as the counter electrode, and a Ag/AgCl electrode (Sigma-Aldrich) as the reference electrode. Measurements were collected by applying a $10\text{ mV}_{\text{rms}}$ sinusoidal voltage at decreasing frequencies from 100 kHz to 1 Hz. Prior to EIS, each device was placed in an 80°C oven for 1 h to remove any potential moisture. EIS was collected on the same devices before and after sterilization.

DC Conductivity. MXtrodies for conductivity measurements were prepared as $\sim 2\text{ cm} \times 2\text{ cm}$ square samples. Thin-film samples were prepared on $3\text{ }\mu\text{m}$ Parylene C coated glass slides spray-coated with 100 mL of 1 mg mL^{-1} $\text{Ti}_3\text{C}_2\text{T}_x$. Spray-coating was performed on a 150°C hot plate, and slides were placed in an 80°C oven for 1 h after film deposition. Conductivity measurements were collected on each thin-film and MXtrode sample before and after sterilization. For MXtrodies, the average thickness of the infused textile prior to encapsulation was found to be consistent with previously reported values, at $0.28 \pm 0.03\text{ mm}$ ($n = 4$).³⁰ Thin-film thickness was measured on a high-resolution profilometer (KLA Tencor P7 2D profilometer) and was $150 \pm 20\text{ nm}$ ($n = 5$). DC conductivity was measured using a Loresla-AX four-point probe. Sheet resistance (Rs , Ω/\square) and film thickness (T , nm) were collected for each sample. Conductivity (σ , S/cm) was calculated as follows:

$$\sigma = \frac{1}{\text{Rs}T} \quad (1)$$

X-ray Diffraction. A Rigaku MiniFlex benchtop X-ray diffractometer was used for XRD measurements (Rigaku Co. Ltd.). The source was Cu $\text{K}\alpha$ ($\lambda = 0.1542\text{ nm}$), and spectra were acquired at 40 kV, 15 mA, for Bragg angles of $3\text{--}60^\circ$ at a rate of 14° min^{-1} with a step of 0.02° . After collection, spectra were fitted using CrystalDiffract to identify peak locations, calculate fwhm, and derive the (002) peak *d*-spacing values.

Raman Spectroscopy. A Renishaw inVia Raman spectrometer (Gloucestershire, UK) instrument was used for all measurements. The acquisition time for the measurements was 10 s using a $63\times$ objective ($\text{NA} = 0.7$). The excitation intensity using the diode (785 nm) laser was $10.5\text{ mW} \times 10\%$. All measurements were conducted by raster scanning from 100 to 3200 cm^{-1} . Additional measurements investigating the presence of adventitious carbons at shift values $> 1000\text{ cm}^{-1}$ were collected using a 514 nm excitation wavelength. After collection, peak amplitude and fwhm peak values were confirmed

using OriginLab, which fitted the peak with a Gaussian curve for calculation. Gaussian fitting for the $\text{A}_{1g}(\text{C})$ peak was calculated using the following equation, where A is the peak amplitude, x_0 is the peak center, sd is the standard deviation of the curve, and H is the baseline offset of the peak.

$$G(x) = Ae^{(x(i)-x_0)^2/(2*\text{sd}^2)} + H \quad (2)$$

X-ray Photoelectron Spectroscopy. XPS was acquired using a PHI VersaProbe 5000 instrument (Physical Electronics) with a 25 W monochromatic Al $\text{K}\alpha$ (1486.6 eV) X-ray source targeting a $200\text{ }\mu\text{m}$ spot. Charge neutralization was acquired through a dual-beam setup using low-energy Ar^+ ions and low-energy electrons at 1 eV and 200 μA . Survey spectra and high-resolution spectra from the Ti 2p and C 1s core-level region were collected using pass energy/energy resolution of 117.4/0.5 and 23.5/0.05 eV, respectively. The binding energy scales were calibrated by adjusting the C–C/C–H component from adventitious carbon in the C 1s spectra to 284.8 eV, where the required shift was $<3.3\text{ eV}$ for all samples. Quantification and peak fitting were conducted using the CasaXPS software following previously published studies.⁵⁶

Optical Microscopy. Optical images of the MXene electrodes were acquired using a Keyence VHX6000 digital microscope. Image magnification ranged from $50\times$ to $200\times$ for MXtrodies and thin-film microelectrodes, respectively. 3D depth composition was performed during image acquisition to resolve the image at multiple depths.

Scanning Electron Microscopy. SEM images of the thin-film microelectrodes and MXtrodies were acquired using a FEI QUANTA 600 FE-SEM machine. Charge neutralization was accomplished with copper conductive grounding tape. Chamber pressure was kept at a constant 0.38 Torr, and power was set to 15 keV during acquisition. Image magnification was in the range $50\text{--}3000\times$ for MXtrodies and thin-film microelectrodes, respectively.

Energy Dispersive X-ray Spectroscopy. EDX spectra of the thin-film microelectrodes and MXtrodies was acquired in the same scanning sessions as the SEM imaging. Samples were charge neutralized with copper conductive tape, and the samples were kept under high vacuum during acquisition. EDX spectra were collected and fitted with elemental mapping using the EDAX Team wavelength dispersive spectrometry analysis system in mapping mode with a final resolution of 256×512 voxels per image. Spectra were normalized by the sum of counts measured within 0–5.5 keV at the end of acquisition.

Mechanical Testing. Cyclic bending and tensile stress/strain measurements were performed using an Instron testing system (Instron 5948). MXtrode samples were prepared with $5\text{ mm} \times 5\text{ cm}$ strips of textile infused with $\text{Ti}_3\text{C}_2\text{T}_x$ MXene ink and encapsulated in PDMS as previously described. After sterilization, samples were placed in the Instron and were subjected to 300 cycles of 20 mm compression to induce bending that corresponded to a bending radius of $\sim 5\text{ mm}$. Throughout testing, resistance was recorded at 2 Hz with a Gamry Reference 600 potentiostat using alligator clips fixed to each end of the sample. Resistance was also measured with a potentiostat before and after testing to assess overall change in resistance as a result of the cyclic deformation. Force–displacement curves were measured by vertically applying force to each sample until failure.

Bacterial Culture and Quantification Assays. *Escherichia coli* ATCC11775 (*E. coli*) was grown and plated in Luria–Bertani (LB) agar plates incubated overnight at 37°C . Following the incubation period, one isolated colony was transferred to 6 mL of medium (LB broth), which was incubated overnight (12–16 h) at 37°C . On the following day, the inoculum was prepared by diluting the bacterial overnight solutions 1:100 in 6 mL of the respective media and incubated at 37°C until logarithmic phase ($\text{OD}_{600} = 0.5$). The devices were then placed in Petri dishes (EtO group) or glass flasks (autoclave group) with 15 mL of LB broth. Groups exposed to bacteria were inoculated with $2 \times 10^6\text{ cells mL}^{-1}$ prior to sterilization. During sterilization, all samples were placed in glass flasks. Three aliquots of each condition (100 μL) were transferred to a 96-well plate, and OD_{600} values were quantified at 0, 0.5, 1, 2, 4, and 24 h

using the Elx808 absorbance microplate reader (Biotek, VT, USA). After OD₆₀₀ values were recorded, 10-fold serial dilutions were performed, and the dilutions were plated on LB agar plates and allowed to grow overnight at 37 °C. Afterward, CFU counts were recorded. H₂O₂ gas plasma bacterial evaluation was not collected due to the damaging oxidation from sterilization, which causes functional degradation to both Ti₃C₂T_x films and devices.

Statistical Analysis. Effect size was used as the primary indication of sterilization-induced degradation. The effect size provides a quantitative indication of changes in impedance and conductivity after sterilization, as opposed to the binary *p*-value indication of whether the data are statistically different in the initial and final cases because it calculates the change in the device performances as a metric of the standard deviation of the presterilization distribution.⁵⁷ The expression of the effect size is shown below, where \bar{x}_1 and \bar{x}_2 are the means, n_1 and n_2 are the sample sizes, and sd_1 and sd_2 are the standard deviations for the pre- and post distributions, respectively. As an additional direct statistical test, we also computed the confidence interval for each pre–post condition, to confirm that significant changes were consistent with the measures of effect size.

$$\text{Cohen's } d_s = \frac{\bar{x}_1 - \bar{x}_2}{\sqrt{\frac{(n_1 - 1)*sd_1^2 + (n_2 - 1)*sd_2^2}{(n_1 + n_2 - 2)}}} \quad (3)$$

ASSOCIATED CONTENT

Data Availability Statement

The data supporting the findings of this study are available upon reasonable request from the authors.

SI Supporting Information

The Supporting Information is available free of charge at <https://pubs.acs.org/doi/10.1021/acsnano.3c01525>.

Schematics of thin-film microelectrodes and MXtrodies; SEM and EDX spectra of thin-film microelectrode and MXtrode contact; EIS of 1, 2.5, and 5 mm MXtrode devices pre- and post-sterilization; Raman spectra of MXtrodies; sterilization-induced Raman A_{1g}(C) peak shape and amplitude change in thin-film microelectrodes and MXtrode devices; blue-shifting and attenuating A_{1g}(C) peak in Raman of H₂O₂-sterilized thin-film samples; XPS survey spectra and core-level Ti 2p and C 1s spectra for thin-film devices and MXtrodies; SEM and EDX spectra of sterilized thin-film contacts; SEM of sterilized MXtrode contacts; cyclic deformation and tensile stress strain curves for MXtrode composites; optical density of bacterial assays; impedance and conductivity values pre- and post-sterilization with effect size and confidence intervals; *d*-spacing and peak location from XRD patterns; quantification from Ti 2p and C 1s curve-fitting of XPS spectra ([PDF](#))

AUTHOR INFORMATION

Corresponding Author

Flavia Vitale — Department of Bioengineering, University of Pennsylvania, Philadelphia, Pennsylvania 19104, United States; Center for Neuroengineering and Therapeutics, Department of Neurology, and Department of Physical Medicine and Rehabilitation, University of Pennsylvania, Philadelphia, Pennsylvania 19104, United States; Center for Neurotrauma, Neurodegeneration, and Restoration, Corporal Michael J. Crescenz Veterans Affairs Medical Center, Philadelphia, Pennsylvania 19104, United States;
Email: vitalef@pennmedicine.upenn.edu

Authors

Spencer R. Averbeck — Department of Bioengineering, University of Pennsylvania, Philadelphia, Pennsylvania 19104, United States; Center for Neuroengineering and Therapeutics, University of Pennsylvania, Philadelphia, Pennsylvania 19104, United States; orcid.org/0000-0002-8273-0087

Doris Xu — Department of Bioengineering, University of Pennsylvania, Philadelphia, Pennsylvania 19104, United States; Center for Neuroengineering and Therapeutics, University of Pennsylvania, Philadelphia, Pennsylvania 19104, United States; orcid.org/0000-0002-4742-0665

Brendan B. Murphy — Department of Bioengineering, University of Pennsylvania, Philadelphia, Pennsylvania 19104, United States; Center for Neuroengineering and Therapeutics, University of Pennsylvania, Philadelphia, Pennsylvania 19104, United States; orcid.org/0000-0003-3021-6286

Kateryna Shevchuk — Department of Material Science and Engineering, Drexel University, Philadelphia, Pennsylvania 19104, United States; AJ Drexel Nanomaterials Institute, Drexel University, Philadelphia, Pennsylvania 19104, United States; orcid.org/0000-0001-7411-3110

Sneha Shankar — Department of Bioengineering, University of Pennsylvania, Philadelphia, Pennsylvania 19104, United States; Center for Neuroengineering and Therapeutics, University of Pennsylvania, Philadelphia, Pennsylvania 19104, United States; orcid.org/0000-0001-9281-5036

Mark Anayee — Department of Material Science and Engineering, Drexel University, Philadelphia, Pennsylvania 19104, United States; AJ Drexel Nanomaterials Institute, Drexel University, Philadelphia, Pennsylvania 19104, United States; orcid.org/0000-0002-6691-920X

Marcelo Der Torossian Torres — Department of Bioengineering, University of Pennsylvania, Philadelphia, Pennsylvania 19104, United States; Department of Chemical and Biomolecular Engineering, University of Pennsylvania, Philadelphia, Pennsylvania 19104, United States; Departments of Psychiatry and Microbiology, Perelman School of Medicine University of Pennsylvania, Philadelphia, Pennsylvania 19104, United States; Institute for Biomedical Informatics, University of Pennsylvania, Philadelphia, Pennsylvania 19104, United States

Michael S. Beauchamp — Department of Neurosurgery, University of Pennsylvania, Philadelphia, Pennsylvania 19104, United States

Cesar de la Fuente-Nunez — Department of Bioengineering, University of Pennsylvania, Philadelphia, Pennsylvania 19104, United States; Department of Chemical and Biomolecular Engineering, University of Pennsylvania, Philadelphia, Pennsylvania 19104, United States; Departments of Psychiatry and Microbiology, Perelman School of Medicine University of Pennsylvania, Philadelphia, Pennsylvania 19104, United States; Institute for Biomedical Informatics, University of Pennsylvania, Philadelphia, Pennsylvania 19104, United States

Yury Gogotsi — Department of Material Science and Engineering, Drexel University, Philadelphia, Pennsylvania 19104, United States; AJ Drexel Nanomaterials Institute, Drexel University, Philadelphia, Pennsylvania 19104, United States; orcid.org/0000-0001-9423-4032

Complete contact information is available at:

<https://pubs.acs.org/10.1021/acsnano.3c01525>

Author Contributions

S.R.A. and F.V. initiated the project. D.X. prepared and characterized a subset of the MXtrode designs. B.B.M. aided in XRD characterization of thin-film and MXtrode films. K.S. and M.A. performed structural characterization before and after sterilization under Y.G.'s supervision. S.S. provided technical support during the design and fabrication of the devices. M.D.T.T. conducted bacterial assays and quantification under C.d.I.F.-N.'s supervision. M.S.B. provided additional supervision throughout the project. S.R.A. wrote the manuscript with contributions from all other authors. F.V. supervised the project.

Notes

The authors declare the following competing financial interest(s): F.V. and Y.G. are co-inventors on international patent application No. PCT/US2018/051084, Implantable devices using 2D metal carbides and nitrides (MXenes). F.V. is a co-inventor on U.S. provisional patent application No. PCT/US2018/051084, Rapid manufacturing of absorbent substrates for soft, conformable sensors and conductors. C.d.I.F.-N. provides consulting services to Invaio Sciences and is a member of the Scientific Advisory Boards of Nowture S.L. and Phare Bio. The remaining authors declare no competing interests.

ACKNOWLEDGMENTS

This work was supported by the National Institutes of Health (NIH) Grant Nos. R01AR081062 (F.V.), R01NS121219 (F.V. and Y.G.), and U01NS113339 (M.S.B.). M.A. was supported by the National Science Foundation 870 Graduate Research Fellowship Program (NSF GRFP) under Grant No. DGE-1646737 and the U.S. Department of Education Graduate Assistance in Areas of National Need (GAANN) fellowship. B.B.M. was supported by the NSF GRFP under Grant No. DGE-1845298. This work was carried out in part at the Singh Center for Nanotechnology, part of the National Nanotechnology Coordinated Infrastructure Program, which is supported by the NSF Grant NNCI-2025608. Any opinions, findings, and conclusions or recommendations expressed in this material are those of the author(s) and do not necessarily reflect the views of the National Science Foundation. C.d.I.F.-N. acknowledges funding from the IADR Innovation in Oral Care Award, the Procter & Gamble Company, United Therapeutics, a BBRF Young Investigator Grant, the Nemirovsky Prize, Penn Health-Tech Accelerator Award, the Dean's Innovation Fund from the Perelman School of Medicine at the University of Pennsylvania, the National Institute of General Medical Sciences of the National Institutes of Health under award number R35GM138201, and the Defense Threat Reduction Agency (DTRA; HDTRA11810041 and HDTRA1-21-1-0014). We thank Dr. Sarah Gullbrand for the help with mechanical testing, Mr. William K. S. Ojemann for an insightful discussion on statistical analysis, the Penn UALAR staff for access and support with plasma sterilization, and MuRata Manufacturing Co. for providing the MXene material.

ABBREVIATIONS

Pt, platinum; EtO, ethylene oxide; n , number of samples/channels; PDMS, polydimethylsiloxane; SEM, scanning

electron microscopy; CFU, colony forming units; EIS, electrochemical impedance spectroscopy; DC, direct current; XRD, X-ray diffraction; XPS, X-ray photoelectron spectroscopy; fwhm, full-width at half-max; OD, optical density; SNR, signal-to-noise ratio

REFERENCES

- (1) Vitale, F.; Litt, B. Bioelectronics: The Promise of Leveraging the Body's Circuitry to Treat Disease. *Bioelectronics in Medicine* **2018**, *1*, 3–7.
- (2) Arya, R.; Wilson, J. A.; Fujiwara, H.; Rozhkov, L.; Leach, J. L.; Byars, A. W.; Rose, D. F. Presurgical Language Localization with Visual Naming Associated ECoG High-Gamma Modulation in Pediatric Drug-Resistant Epilepsy. *Epilepsia* **2017**, *58*, 663–673.
- (3) Okun, M. S. Deep-Brain Stimulation for Parkinson's Disease. *New England Journal of Medicine* **2012**, *367*, 1529–1538.
- (4) Mayberg, H. S.; Lozano, A. M.; Voon, V.; McNeely, H. E.; Seminowicz, D.; Hamani, C.; Kennedy, S. H. Deep Brain Stimulation for Treatment-Resistant Depression. *Neuron* **2005**, *45*, 651–660.
- (5) Frigo, C.; Crenna, P. Multichannel SEMG in Clinical Gait Analysis: A Review and State-of-the-Art. *Clinical Biomechanics* **2009**, *24*, 236–245.
- (6) Dhanasingh, A.; Jolly, C. An Overview of Cochlear Implant Electrode Array Designs. *Hearing Research* **2017**, *356*, 93–103.
- (7) Taplin, A. M.; de Pesters, A.; Brunner, P.; Hermes, D.; Dalfino, J. C.; Adamo, M. A.; Schalk, G. Intraoperative Mapping of Expressive Language Cortex using Passive Real-Time Electrocorticography. *Epilepsy & Behavior Case Reports* **2016**, *5*, 46–51.
- (8) Sahyouni, R.; Chang, D. T.; Moshtaghi, O.; Mahmoodi, A.; Djalilian, H. R.; Lin, H. W. Functional and Histological Effects of Chronic Neural Electrode Implantation. *Laryngoscope Investigative Otolaryngology* **2017**, *2*, 80–93.
- (9) Harris, A. R. Current Perspectives on the Safe Electrical Stimulation of Peripheral Nerves with Platinum Electrodes. *Bioelectronics in Medicine* **2020**, *3*, 37–49.
- (10) Wellman, S. M.; Eles, J. R.; Ludwig, K. A.; Seymour, J. P.; Michelson, N. J.; McFadden, W. E.; Kozai, T. D. A Materials Roadmap to Functional Neural Interface Design. *Adv. Funct. Mater.* **2018**, *28*, 1701269.
- (11) Patel, P. R.; Welle, E. J.; Letner, J. G.; Shen, H.; Bullard, A. J.; Caldwell, C. M.; Chestek, C. A. Utah Array Characterization and Histological Analysis of a Multi-Year Implant in Non-Human Primate Motor and Sensory Cortices. *Journal of Neural Engineering* **2023**, *20*, 014001.
- (12) Garg, R.; Gopalan, D. P.; de la Barrera, S. C.; Hafiz, H.; Nuhfer, N. T.; Viswanathan, V.; Cohen-Karni, T. Electron Transport in Multidimensional Fuzzy Graphene Nanostructures. *Nano Lett.* **2019**, *19*, 5335–5339.
- (13) Driscoll, N.; Rosch, R. E.; Murphy, B. B.; Ashourvan, A.; Vishnubhotla, R.; Dickens, O. O.; Vitale, F. Multimodal in Vivo Recording using Transparent Graphene Microelectrodes Illuminates Spatiotemporal Seizure Dynamics at the Microscale. *Communications Biology* **2021**, *4*, 1–14.
- (14) Lu, Y.; Lyu, H.; Richardson, A. G.; Lucas, T. H.; Kuzum, D. Flexible Neural Electrode Array Based on Porous Graphene for Cortical Microstimulation and Sensing. *Sci. Rep.* **2016**, *6*, 1–9.
- (15) Wang, K.; Fishman, H. A.; Dai, H.; Harris, J. S. Neural Stimulation with a Carbon Nanotube Microelectrode Array. *Nano Lett.* **2006**, *6*, 2043–2048.
- (16) Lu, L.; Fu, X.; Liew, Y.; Zhang, Y.; Zhao, S.; Xu, Z.; Duan, X. Soft and MRI Compatible Neural Electrodes from Carbon Nanotube Fibers. *Nano Lett.* **2019**, *19*, 1577–1586.
- (17) Simpson, D. A.; Morrisroe, E.; McCoey, J. M.; Lombard, A. H.; Mendis, D. C.; Treussart, F.; Hollenberg, L. C. Non-Neurotoxic Nanodiamond Probes for Intraneuronal Temperature Mapping. *ACS Nano* **2017**, *11*, 12077–12086.
- (18) Tchoe, Y.; Bourhis, A. M.; Cleary, D. R.; Stedelin, B.; Lee, J.; Tonsfeldt, K. J.; Dayeh, S. A. Human Brain Mapping with

- Multithousand-Channel PtNRGrids Resolves Spatiotemporal Dynamics. *Science Translational Medicine* **2022**, *14*, 1441.
- (19) Driscoll, N.; Dong, R.; Vitale, F. Emerging Approaches for Sensing and Modulating Neural Activity Enabled by Nanocarbons and Carbides. *Curr. Opin. Biotechnol.* **2021**, *72*, 76–85.
- (20) Garg, R.; Vitale, F. Latest Advances on MXenes in Biomedical Research and Healthcare. *MRS Bull.* **2023**, *48*, 283.
- (21) Vitale, F.; Driscoll, N.; Murphy, B. B. Biomedical Applications of MXenes. In *2D Metal Carbides and Nitrides (MXenes)*; Anasori, B.; Gogotsi, Y., Eds.; Springer: Cham, 2019; pp 503–524.
- (22) Kim, S. J.; Koh, H. J.; Ren, C. E.; Kwon, O.; Maleski, K.; Cho, S. Y.; Jung, H. T. Metallic $Ti_3C_2T_x$ MXene Gas Sensors with Ultrahigh Signal-to-Noise Ratio. *ACS Nano* **2018**, *12*, 986–993.
- (23) Xie, X.; Zhao, M. Q.; Anasori, B.; Maleski, K.; Ren, C. E.; Li, J.; Gogotsi, Y. Porous Heterostructured MXene/Carbon Nanotube Composite Paper with High Volumetric Capacity for Sodium-Based Energy Storage Devices. *Nano Energy* **2016**, *26*, 513–523.
- (24) Alhabeb, M.; Maleski, K.; Anasori, B.; Lelyukh, P.; Clark, L.; Sin, S.; Gogotsi, Y. Guidelines for Synthesis and Processing of Two-Dimensional Titanium Carbide ($Ti_3C_2T_x$ MXene). *Chem. Mater.* **2017**, *29*, 7633–7644.
- (25) Dai, C.; Lin, H.; Xu, G.; Liu, Z.; Wu, R.; Chen, Y. Biocompatible 2D Titanium Carbide (MXenes) Composite Nanosheets for pH-Responsive MRI-Guided Tumor Hyperthermia. *Chem. Mater.* **2017**, *29*, 8637–8652.
- (26) Rasool, K.; Mahmoud, K. A.; Johnson, D. J.; Helal, M.; Berdiyorov, G. R.; Gogotsi, Y. Efficient Antibacterial Membrane Based on Two-Dimensional $Ti_3C_2T_x$ (MXene) Nanosheets. *Sci. Rep.* **2017**, *7*, 1–11.
- (27) Rasool, K.; Helal, M.; Ali, A.; Ren, C. E.; Gogotsi, Y.; Mahmoud, K. A. Antibacterial Activity of $Ti_3C_2T_x$ MXene. *ACS Nano* **2016**, *10*, 3674–3684.
- (28) Seyedin, S.; Uzun, S.; Levitt, A.; Anasori, B.; Dion, G.; Gogotsi, Y.; Razal, J. M. MXene Composite and Coaxial Fibers with High Stretchability and Conductivity for Wearable Strain Sensing Textiles. *Adv. Funct. Mater.* **2020**, *30*, 1910504.
- (29) Murphy, B. B.; Mulcahey, P. J.; Driscoll, N.; Richardson, A. G.; Robbins, G. T.; Apollo, N. V.; Vitale, F. A Gel-Free $Ti_3C_2T_x$ -Based Electrode Array for High-Density, High-Resolution Surface Electromyography. *Advanced Materials Technologies* **2020**, *5*, 2000325.
- (30) Driscoll, N.; Erickson, B.; Murphy, B. B.; Richardson, A. G.; Robbins, G.; Apollo, N. V.; Vitale, F. MXene-Infused Bioelectronic Interfaces for Multiscale Electrophysiology and Stimulation. *Science Translational Medicine* **2021**, *13*, 8629.
- (31) Driscoll, N.; Richardson, A. G.; Maleski, K.; Anasori, B.; Adewole, O.; Lelyukh, P.; Vitale, F. Two-Dimensional Ti_3C_2 MXene for High-Resolution Neural Interfaces. *ACS Nano* **2018**, *12*, 10419–10429.
- (32) Driscoll, N.; Maleski, K.; Richardson, A. G.; Murphy, B. B.; Anasori, B.; Lucas, T. H.; Vitale, F. Fabrication of Ti_3C_2 MXene Microelectrode Arrays for *in vivo* Neural Recording. *JoVE (Journal of Visualized Experiments)* **2020**, *156*, No. e60741.
- (33) Ni, M.; Chen, J.; Wang, C.; Wang, Y.; Huang, L.; Xiong, W.; Fei, J. A High-Sensitive Dopamine Electrochemical Sensor Based on Multilayer Ti_3C_2 MXene, Graphitized Multi-Walled Carbon Nanotubes and ZnO Nanospheres. *Microchemical Journal* **2022**, *178*, 107410.
- (34) Shahzad, F.; Iqbal, A.; Zaidi, S. A.; Hwang, S. W.; Koo, C. M. Nafion-Stabilized Two-Dimensional Transition Metal Carbide ($Ti_3C_2T_x$ MXene) as a High-Performance Electrochemical Sensor for Neurotransmitter. *Journal of Industrial and Engineering Chemistry* **2019**, *79*, 338–344.
- (35) Wang, Y.; Garg, R.; Hartung, J. E.; Goad, A.; Patel, D. A.; Vitale, F.; Cohen-Karni, T. $Ti_3C_2T_x$ MXene Flakes for Optical Control of Neuronal Electrical Activity. *ACS Nano* **2021**, *15*, 14662–14671.
- (36) Rutala, W. A.; Weber, D. J. Guideline for Disinfection and Sterilization in Healthcare Facilities. *Healthcare Infection Control Practices Advisory Committee (HICPAC), Center for Disease Control (CDC)*, 2008, <https://stacks.cdc.gov/view/cdc/47378>.
- (37) Jagadeeswaran, I.; Chandran, S. ISO 11135: Sterilization of Health-Care Products—Ethylene Oxide, Requirements for Development, Validation and Routine Control of a Sterilization Process for Medical Devices. In *Medical Device Guidelines and Regulations Handbook* Cham; Springer International Publishing: 2022; pp 145–153.
- (38) Garg, R.; Driscoll, N.; Shankar, S.; Hullfish, T.; Anselmino, F.; Iberite, F.; Averbeck, S.; Vitale, F. Wearable High-Density MXene-Bioelectronics for Neuromuscular Diagnostics, Rehabilitation, and Assistive Technologies. *Small Methods* **2022**, 2201318.
- (39) Boehler, C.; Carli, S.; Fadiga, L.; Stieglitz, T.; Asplund, M. Tutorial: Guidelines for Standardized Performance Tests for Electrodes Intended for Neural Interfaces and Bioelectronics. *Nat. Protoc.* **2020**, *15*, 3557–3578.
- (40) Franks, W.; Schenker, I.; Schmutz, P.; Hierlemann, A. Impedance Characterization and Modeling of Electrodes for Biomedical Applications. *IEEE Transactions on Biomedical Engineering* **2005**, *52*, 1295–1302.
- (41) Li, Z.; Wang, L.; Sun, D.; Zhang, Y.; Liu, B.; Hu, Q.; Zhou, A. Synthesis and Thermal Stability of Two-Dimensional Carbide MXene Ti_3C_2 . *Materials Science and Engineering* **2015**, *191*, 33–40.
- (42) Holder, C. F.; Schaak, R. E. Tutorial on Powder X-ray Diffraction for Characterizing Nanoscale Materials. *ACS Nano* **2019**, *13*, 7359–7365.
- (43) Lotfi, R.; Naguib, M.; Yilmaz, D. E.; Nanda, J.; Van Duin, A. C. A Comparative Study on the Oxidation of Two-Dimensional Ti_3C_2 MXene Structures in Different Environments. *Journal of Materials Chemistry A* **2018**, *6*, 12733–12743.
- (44) Ahmed, B.; Anjum, D. H.; Hedhili, M. N.; Gogotsi, Y.; Alshareef, H. N. H_2O_2 Assisted Room Temperature Oxidation of Ti_2C MXene for Li-ion Battery Anodes. *Nanoscale* **2016**, *8*, 7580–7587.
- (45) Sarycheva, A.; Gogotsi, Y. Raman Spectroscopy Analysis of the Structure and Surface Chemistry of $Ti_3C_2T_x$ MXene. *Chem. Mater.* **2020**, *32*, 3480–3488.
- (46) Rakhi, R. B.; Ahmed, B.; Hedhili, M. N.; Anjum, D. H.; Alshareef, H. N. Effect of Post-Etch Annealing Gas Composition on the Structural and Electrochemical Properties of Ti_2CT_x MXene Electrodes for Supercapacitor applications. *Chem. Mater.* **2015**, *27*, 5314–5323.
- (47) Johnson, D.; Hansen, K.; Yoo, R.; Djire, A. Elucidating the Charge Storage Mechanism on Ti_3C_2 MXene through In Situ Raman Spectroelectrochemistry. *ChemElectroChem.* **2022**, *9*, No. e202200555.
- (48) Ghassemi, H.; Harlow, W.; Mashtalar, O.; Beidaghi, M.; Lukatskaya, M. R.; Gogotsi, Y.; Taheri, M. L. In Situ Environmental Transmission Electron Microscopy Study of Oxidation of Two-Dimensional Ti_3C_2 and Formation of Carbon-Supported TiO_2 . *Journal of Materials Chemistry A* **2014**, *2*, 14339–14343.
- (49) Adar, F.; Lee, E.; Mamedov, S.; Whitley, A. Experimental Evaluation of the Depth Resolution of a Raman Microscope. *Microscopy and Microanalysis* **2010**, *16*, 360–361.
- (50) Biesinger, M. C.; Payne, B. P.; Grosvenor, A. P.; Lau, L. W.; Gerson, A. R.; Smart, R. S. C. Resolving Surface Chemical States in XPS Analysis of First Row Transition Metals, Oxides and Hydroxides: Cr, Mn, Fe, Co and Ni. *Appl. Surf. Sci.* **2011**, *257*, 2717–2730.
- (51) Shuck, C. E.; Sarycheva, A.; Anayee, M.; Levitt, A.; Zhu, Y.; Uzun, S.; Gogotsi, Y. Scalable Synthesis of $Ti_3C_2T_x$ MXene. *Adv. Eng. Mater.* **2020**, *22*, 1901241.
- (52) Chae, Y.; Kim, S. J.; Cho, S. Y.; Choi, J.; Maleski, K.; Lee, B. J.; Ahn, C. W. An Investigation into the Factors Governing the Oxidation of Two-Dimensional Ti_3C_2 MXene. *Nanoscale* **2019**, *11*, 8387–8393.
- (53) Uguz, I.; Ganji, M.; Hama, A.; Tanaka, A.; Inal, S.; Youssef, A.; Malliaras, G. G. Autoclave Sterilization of PEDOT: PSS Electrophysiology Devices. *Adv. Healthcare Mater.* **2016**, *5*, 3094–3098.

- (54) Chiang, C. H.; Won, S. M.; Orsborn, A. L.; Yu, K. J.; Trumpis, M.; Bent, B.; Viventi, J.; et al. Development of a Neural Interface for High-Definition, Long-term Recording in Rodents and Nonhuman Primates. *Science Translational Medicine* **2020**, *12*, No. eaay4682.
- (55) Michałowski, P. P.; Anayee, M.; Mathis, T. S.; Kozdra, S.; Wójcik, A.; Hantanasirisakul, K.; Gogotsi, Y.; et al. Oxycarbide MXenes and MAX Phases Identification using Monoatomic Layer-by-Layer Analysis with Ultralow-Energy Secondary-Ion Mass Spectrometry. *Nat. Nanotechnol.* **2022**, *17*, 1192–1197.
- (56) Näslund, L. Å.; Persson, I. XPS Spectra Curve Fittings of $Ti_3C_2T_x$ Based on First Principles Thinking. *Appl. Surf. Sci.* **2022**, *593*, 153442.
- (57) Nakagawa, S.; Cuthill, I. C. Effect Size, Confidence Interval and Statistical Significance: A Practical Guide for Biologists. *Biological Reviews* **2007**, *82*, 591–605.

□ Recommended by ACS

Ultrastrong yet Ductile 2D Titanium Nanomaterial for On-Skin Conformal Triboelectric Sensing

Minhyuk Park, Yong Yang, et al.

JUNE 14, 2023

NANO LETTERS

READ ▶

Wireless, Fully Implantable and Expandable Electronic System for Bidirectional Electrical Neuromodulation of the Urinary Bladder

Joong Hoon Lee, Suk-Won Hwang, et al.

APRIL 18, 2023

ACS NANO

READ ▶

An Intelligent Wearable Filtration System for Health Management

Shuo Shi, Jinlian Hu, et al.

MARCH 30, 2023

ACS NANO

READ ▶

Moving beyond $Ti_2C_3T_x$ MXene to Pt-Decorated $TiO_2@TiC$ Core–Shell via Pulsed Laser in Reshaping Modification for Accelerating Hydrogen Evolution Kinetics

Chae Eun Park, Myong Yong Choi, et al.

MARCH 06, 2023

ACS NANO

READ ▶

[Get More Suggestions >](#)